

Realization of room-temperature ferromagnetic semiconducting state in graphene monolayer

Yu Zhang^{1,§}, Xue-Lei Sui^{2,§}, Dong-Lin Ma¹, Wen-Hui Duan², and Lin He^{1,*}

¹Center for Advanced Quantum Studies, Department of Physics, Beijing Normal University, Beijing, 100875, People's Republic of China

²State Key Laboratory of Low-Dimensional Quantum Physics and Collaborative Innovation Center of Quantum Matter, Department of Physics, Tsinghua University, Beijing 100084, People's Republic of China

* Email: helin@bnu.edu.cn

Room-temperature ferromagnetic semiconductor is vital in nonvolatile digital circuits and it can provide an idea system where we can make use of both charge and spin of electrons. However, seeking room-temperature ferromagnetic semiconductors is still just an appealing idea that has never been realized in practice up to now. Here we demonstrate that graphene monolayer, hybridized with underlying Ni substrate, is the room-temperature ferromagnetic semiconductor that has been continuously searched for decades. Our spin-polarized scanning tunnelling microscopy (STM) experiments, complemented by first-principles calculations, demonstrate explicitly that the interaction between graphene and the Ni substrate generates a large gap in graphene and simultaneously leads to a relatively shift between majority- and minority-spin bands. Consequently, the graphene sheet on Ni substrate exhibits a spin-polarized gap with energy of several tens meV even at room-temperature. This result makes the science and applications of room-temperature ferromagnetic semiconductors achievable and raises hopes of graphene-based novel information technologies.

Ferromagnetic semiconductors, taking great advantages of both charge and spin degree of freedom of electrons, open up possibilities for new semiconductor-based data processing and memory applications^{1,2}. During the past decades, looking for high Curie-temperature (T_C) ferromagnetic semiconductors, especially for those with the ferromagnetism persisting above room-temperature, has attracted immense research interest. There are two general strategies to achieve this objective. A straightforward method is to directly synthesize gapped materials with high T_C ferromagnetism. Stoichiometric EuO is one of the rare obtained intrinsic ferromagnetic semiconductors with the record high Curie temperature of $\sim 69\text{ K}$ ³⁻⁵. Although it was predicted to host many promising properties (such as the nearly 100% spin-polarized current), the relatively low T_C and instability in air hinder its application⁵. Another available method is to introduce a high concentration of magnetic ions into nonmagnetic semiconductors⁶. According to the meanfield p - d Zener model⁶, the T_C of the diluted magnetic semiconductors (DMSs) depends tightly on the magnetic impurity concentration x and hole concentration p (carrier mobility) as $T_C \propto xp^{1/3}$. Several well-established DMSs⁷⁻¹⁵, such as (In,Mn)As and (Ga,Mn)As), have been realized successfully and demonstrated experimentally to be robust ferromagnetic semiconductors. However, due to the low solubility of magnetic elements and the immature technology to highly concentrate the magnetic ions at present, the obtained highest T_C of the ferromagnetic semiconductors is still lower than 200 K up to now. Therefore, after seeking for several decades with great efforts, the realization of room-temperature ferromagnetic semiconductors seems to become a science fiction that is beyond the grasp of today's technology.

Both the said two strategies try to induce room-temperature ferromagnetic semiconductor state in the whole ultimate material. However, it was demonstrated to be almost impossible in practice. Here, we report a new recipe to achieve this goal by only driving a small part of an artificial system into the room-temperature ferromagnetic semiconductor state. Our work demonstrates that graphene monolayer on Ni substrate is the room-temperature ferromagnetic semiconductor that scientists

dream to realize it for decades. Pristine graphene is a diamagnetic semimetal¹⁶. Recently, many groups attempt to introduce magnetism in graphene¹⁷⁻²⁸. For example, it has been demonstrated explicitly that graphene with atomic defects and hydrogen chemisorption defects could exhibit localized magnetic moments. However, it is almost impossible to realize macroscopic room-temperature spin-polarized semiconductor band structure in graphene by simply introducing adatoms or atomic vacancies. The recipe reported in this work could overcome this difficulty completely. Once synthesized graphene monolayer on Ni substrate, the electronic structure of graphene π band is strongly perturbed by d electrons of Ni. The π - d interaction not only opens up a gap ($E_{\sigma\uparrow}$ and $E_{\sigma\downarrow}$ for the spin-up and spin-down electrons, respectively) of several hundreds meV in graphene, but also lifts the degeneracy of the majority- and minority-spin bands around K point of graphene²⁹, thus realizing the spin-polarized ferromagnetic semiconducting state with the gap of tens meV in graphene. Very recently, the local magnetic moments of atomic defects in graphene and the emergence of edge magnetism in individual zigzag graphene nanoribbon are studied successfully by measuring their electronic structures via scanning tunnelling microscopy (STM)^{17-20,22-24}. Here, we use spin-polarized STM measurements, for the first time, to directly measure both the relatively energy shift between the majority- and minority-spin bands and the gap opening of the graphene monolayer on Ni substrate. These results provide clearly signatures of the emergence of the room-temperature ferromagnetic state in the graphene monolayer on Ni substrate.

In this paper, the graphene monolayer was grown on a 25 μm -thick Ni foil via a traditional low pressure chemical vapor deposition (LPCVD) method³⁰⁻³² (the X-ray diffraction result and growth method are shown in methods and Supplementary Figure 1 and 2). The thickness of the graphene on Ni foil is well controlled by the growth time, the cooling rate, and the flow ratio of gases. In our experiment, the thickness of the as-grown graphene is characterized by Raman spectra measurements³⁰⁻³³. Two peaks at 1580 cm^{-1} and 2700 cm^{-1} in the Raman spectra (Supplementary Fig. 3) are the G-band and 2D-band respectively, which are the characteristic Raman peaks of graphene. We identify the layer number by comparing the intensity of the G-band and 2D-band.

Figure 1a shows the Raman mapping of I_{2D}/I_G of the synthesized graphene transferred to a 300 nm SiO_2/Si substrate, indicating that the obtained sample under the growth process is mainly graphene monolayer (see Figure S3 of Supplemental Material for more experimental data of samples with different graphene layers). Such a result is further confirmed by our STM measurements. Figure 1b shows a representative $60 \text{ nm} \times 60 \text{ nm}$ STM topographic image of the graphene monolayer on Ni substrate. The quasi-periodic protuberances (with average period of $\sim 10 \text{ nm}$) are the Moiré patterns that are generated by the lattice mismatch ($\sim 1.2\%$) between surface of Ni (111) and graphene. The variation of the protuberances may arise from the roughness of the Ni surface. According to the period of the Moiré patterns, the rotation angle between graphene and Ni (111) surface is estimated to be 1.4° .

Figure 1c shows a typical atomic resolution STM image of the graphene on Ni (111) surface, exhibiting enormous intensity imbalance between the *A* and *B* sublattices. Such a result indicates the inversion symmetry breaking of graphene by the substrate. For graphene on Ni (111) surface, the carbon atoms of the *A* sublattice are mainly on top of the Ni atoms of the topmost atomic layer, while atoms of the *B* sublattice are mainly located above the hollow sites of the topmost atomic layer of Ni due to their minor lattice mismatch, as schematically shown in Fig. 1d. We will demonstrate subsequently that the strong chemical interaction between graphene and Ni substrate not only results in the enormous sublattice asymmetry, but also dramatically changes the electronic band structure of graphene.

Figure 2a shows several representative scanning tunneling spectroscopy (STS) spectra of the graphene monolayer on Ni (111) surface recorded at different temperatures. The slight variation of the spectra is mainly due to the fact that they are not measured exactly at the same position (we will discuss the spatial variation of the gap in Fig. 4). It is interesting to note that we observe a finite gap in the graphene monolayer and the gap persists even at room temperature (300 K). Similar spectra are obtained in all the synthesized graphene monolayer on Ni (111) surface with several different STM tips, which removes any possible artificial effects as the origin of the observed result. To further confirm the gap of the graphene monolayer on Ni (111)

surface, we measured spectra on an insulating hexagonal boron nitride (hBN) monolayer on Cu foil for comparison. In the hBN/Cu system, we clearly observed the large band gap, ~ 5.9 eV, of the hBN monolayer (see Supplementary Figure 4). This indicates that the STM predominantly probes the electronic states of the topmost layer underneath the STM tip and the observed gap in Fig. 2a reflects the electronic structure of the graphene monolayer on Ni surface^{29,34}. In order to explore the effect of the Ni (111) surface on the emergence of the gap in graphene, we measured spectra of graphene monolayer on several different metallic substrates (Cu, Ag, and Rh foils³⁵⁻³⁸) for comparison. All the spectra exhibit V-shaped curves and there is no measurable band gap (see Supplementary Figure 4), as expected to be observed for the pristine graphene monolayer. This demonstrated explicitly that the strong chemical interaction between graphene and Ni substrate is vital for the emergence of the gap in graphene.

The observation of a finite gap in graphene on the Ni (111) surface is quite reasonable since that the substrate generates enormous sublattice asymmetry in graphene (Fig. 1c), which is expected to open a gap in it³⁹⁻⁴³. However, with considering the strong chemical interaction between graphene and Ni and the observed large sublattice imbalance in graphene, the obtained gap, $E_{gap} < 100$ meV, in the graphene monolayer (Fig. 2a) is unexpectedly small. The observed gap is only comparable to the expected gap for a graphene monolayer on hBN substrate^{40,41}, whereas the interaction between graphene and hBN is much weaker than that between graphene and Ni. To fully understand the electronic structure of the graphene monolayer on Ni (111) surface, we carried out first-principles calculations on this system. Figure 2b shows a representative theoretical electronic band structure of the graphene monolayer on Ni (111) surface and the inset of Fig. 2b shows the calculated STM image of the graphene monolayer on Ni (111) surface. Obviously, the strong chemical interaction between graphene and Ni substrate results in the enormous sublattice asymmetry in graphene, as observed in our experiment. The enormous sublattice asymmetry generates a quite large gap (≥ 300 meV) in graphene, labelled as $E_{\sigma\uparrow}$ and $E_{\sigma\downarrow}$ for the spin-up and spin-down electrons respectively in Fig. 2b. Importantly, the strong π - d interaction between graphene and Ni not only opens up a large gap in graphene, but also lifts the degeneracy of the

majority- and minority-spin bands around the K point of graphene, as shown in Fig. 2b. According to our calculation, the spin splitting of the graphene's conduction band is about 300 meV (similar for the valence band). The coexistence of the two effects (the gap opening and the spin splitting) induced by the Ni substrate lead to the realization of the spin-polarized ferromagnetic semiconducting state with the gap of several tens meV in graphene, as schematically shown in Fig. 2c, which agrees well with our observations in the experiment. Since we observe the gap even at room-temperature, our results, therefore, indicate that the graphene monolayer on Ni (111) surface is the room-temperature ferromagnetic semiconductor.

To further confirm the above result, we carried out spin-polarized STM measurements, which provide us unprecedented opportunities to further identify the origin of the gap by directly detecting the majority- and minority-spin bands of graphene separately (Fig. 3)^{44,45}. In our experiment, we used electrochemically etched Ni tips (see Supplementary Figure 5) as the spin-polarized tip⁴⁶. Due to the weak magnetocrystalline anisotropy of Ni⁴⁷, the magnetic polarization of the tip is always along the STM tip, i.e., perpendicular to the surface of the sample. Before the STM measurements, a magnetic field of $B = 2.0$ T ($B = -2.0$ T) perpendicular to the surface of the sample was applied on and then removed gradually to obtain an up-polarized (down-polarized) STM tip. Then, a magnetic field $B = 0.2$ T, which is smaller than the reversal field of the tip, is applied on the sample to make sure that the spins of the sample are aligning along the STM tip (either parallel or antiparallel), as shown in Fig. 3a. Because of the spin conservation during the elastic electron tunnelling, we can detect the spin-up and spin-down bands of graphene separately, as schematically shown in Fig. 3b. In the case that the magnetizations of the STM tip and the sample are parallel, the measured tunneling spectrum mainly reflects the local density-of-state (LDOS) of the spin-up electrons in the sample. In the other case that the magnetic polarizations of the tip and the sample are antiparallel, the recorded dI/dV spectrum is primarily contributed by the LDOS of the spin-down electrons in the sample.

Figure 3c shows two representative spin-resolved dI/dV spectra of the graphene monolayer on Ni foil probed according to the above method (see Supplementary Figure

7 for more experimental results). One spectrum is measured when the spin polarizations of the tip and the sample are parallel, the other is recorded when they are antiparallel. Very similar spectra have been obtained and verified by using several different Ni tips in our experiment (see Supplementary Figure 8). Obviously, both spectra exhibit quite large gaps ~ 300 meV, indicating that the strong interaction between graphene and Ni substrate really generates large gaps, $E_{\sigma\uparrow}$ and $E_{\sigma\downarrow}$, for both the spin-up and spin-down electrons in the graphene. Moreover, there is quite a large shift between the charge neutrality points (CNPs) of the spin-up and spin-down bands. The overlap between the $E_{\sigma\uparrow}$ and $E_{\sigma\downarrow}$ is much smaller than the gaps for either the spin-up or spin-down electrons. As a consequence, we can only detect a gap of several tens meV in graphene by using the non-magnetic STM tip, as shown in Fig. 3c. Our experimental result demonstrated explicitly that the joint effects of the gap opening and the spin splitting induced by the Ni substrate lead to the realization of the spin-polarized ferromagnetic semiconducting state in graphene.

Figure 4a shows three typical STS spectra recorded on different positions of the graphene monolayer at room temperature by using a non-magnetic STM tip. It is interesting to note that both the gap E_{gap} and the CNP of the graphene monolayer depend sensitively on the recorded position. We attribute such a result to the roughness of the Ni surface, which in turn affects the distance, d , between the graphene sheet and Ni surface. To explore effects of the distance on the electronic property, we calculated the electronic band structure of the graphene monolayer on Ni (111) surface with various d , ranging from 0.222 nm to 0.247 nm. Figure 4b and 4c show two representative results (more theoretical results are given in Supplementary Figure 9). Obviously, the distance affects both the gap opening and the spin splitting of the electronic band structure in the graphene monolayer. Therefore, it influences both the gap E_{gap} and the CNP of the graphene monolayer on Ni surface. In Fig. 4d, we plot the gap E_{gap} as a function of the CNP of the graphene monolayer measured in our experiment. The theoretical relationships among the gap E_{gap} , the CNP, and the distance d are also summarized in Fig. 4d. The main feature of the experimental result is reproduced well by the theoretical calculation, which indicates that the spatial variation of the gap E_{gap} and the

CNP of the graphene monolayer on Ni surface is mainly affected by the distance between the graphene sheet and Ni surface. With considering the roughness of the Ni surface, the observed spatial variation of the electronic structures of the graphene monolayer is quite reasonable. In Fig. 4d, the calculated gaps are generally smaller than the measured ones, which may arise from the fact that the LDA calculations usually underestimate the band gap^{48,49}.

In summary, we demonstrate, via spin-polarized STM measurements, that the strong interaction between graphene and Ni substrate generates a large gap in graphene and simultaneously leads to a relatively shift between the majority- and minority-spin bands. Consequently, the graphene sheet on Ni substrate exhibits a spin-polarized semiconductor band structure even at room temperature. Although the whole system is not a ferromagnetic semiconductor, our result indicates that it is facile to realize the room-temperature ferromagnetic state in a part of the artificial system. This may raise hopes of graphene-based novel technologies in the near future.

Methods:

STM/STS measurements. The scanning tunneling microscopy (STM) systems were ultrahigh vacuum scanning probe microscope from UNISOKU. The experimental data were acquired at liquid-helium temperature at ~4.2 K on the STM systems of USM-1300 and USM-1500, and at 77 K and 300 K on the STM systems of USM-1400. All the STM and STS measurements were performed in the ultrahigh vacuum chamber ($\sim 10^{-11}$ Torr) with constant-current scanning mode. The nonmagnetic STM tips were obtained by chemical etching from a wire of Pt (80%)-Ir (20%) alloys, and the spin-polarized STM tips were obtained by electrochemically etched polycrystalline Ni wire (see Figure S5). Lateral dimensions observed in the STM images were calibrated using a standard graphene lattice and a Si (111)-(7 \times 7) lattice and Ag (111) surface. The dI/dV measurements were taken with a standard lock-in technique by turning off the feedback circuit and using a 793-Hz 5 mV a.c. modulation of the tunneling bias.

Sample preparation of graphene monolayer on Ni foil. A traditional ambient

pressure chemical vapor deposition (APCVD) method was adopted to grow graphene monolayer on Ni foil. The polycrystalline Nickel (Ni) foil, which is mainly (111) oriented according to our X-ray diffraction measurements, was first heated from room temperature to 1030°C in 40 min under an argon (Ar) flow of 100 SCCM and hydrogen (H₂) flow of 50 SCCM, and keep this temperature and flow ratio for 20 min. Next methane (CH₄) gas was introduced with a flow ratio of 5 SCCM, and the growth time is 15 min and then cooled down to room temperature (see Figure S2).

References

1. Ohno, H. Making nonmagnetic semiconductors ferromagnetic. *Science* **281**, 951-956 (1998).
2. Ando, K. Seeking Room-Temperature Ferromagnetic Semiconductors. *Science* **312**, 1883-1885 (2006).
3. McGuire, T. R., & Shafer, M. W. Ferromagnetic europium compounds. *J. Appl. Phys.* **35**, 984-988 (1964).
4. Matthias, B. T., Bozorth, R. M., & Van Vleck, J. H. Ferromagnetic interaction in EuO. *Phys. Rev. Lett.* **7**, 160-161 (1961).
5. Schmehl, A., Vaithyanathan, V., Herrnberger, A., Thiel, S., Richter, C., Liberati, M., Heeg, T., Rockerath, M., Kourkoutis, L. F., Muhlbauer, S., Boni, P., Muller, D. A., Barash, Y., Schubert, J., Idzerda, Y., Mannhart, J., & Schlom, D. G. Epitaxial integration of the highly spin-polarized ferromagnetic semiconductor EuO with silicon and GaN. *Nat. Mater.* **6**, 882-887 (2007).
6. Dietl, T., Ohno, H., Matsukura, F., Cibert, J., & Ferrand, D. Zener Model Description of Ferromagnetism in Zinc-Blende Magnetic Semiconductors. *Science* **287**, 1019-1022 (2000).
7. Jungwirth, T., Sinova, J., Masek, J., Kucera, J., & MacDonald, A. H. Theory of ferromagnetic (III,Mn)V semiconductors. *Rev. Mod. Phys.* **78**, 809-864 (2006).
8. Jungwirth, T., Wang, K. Y., Masek, J., Edmonds, K. W., König, J., Sinova, J., Polini,

- M., Goncharuk, N. A., MacDonald, A. H., Sawicki, M., Rushforth, A. W., Campion, R. P., Zhao, L. X., Foxon, C. T., & Gallagher, B. L. Prospects for high temperature ferromagnetism in (Ga,Mn)As semiconductors. *Phys. Rev. B* **72**, 165204 (2005).
9. MacDonald, A. H., Schiffer, P., & Samarth, N. Ferromagnetic semiconductors: moving beyond (Ga,Mn)As. *Nat. Mater.* **4**, 195-202 (2005).
 10. Chen, L., Yang, X., Yang, F., Zhao, J., Misuraca, J., Xiong, P., & Von Molnár, S. (2011). Enhancing the Curie temperature of ferromagnetic semiconductor (Ga, Mn) As to 200 K via nanostructure engineering. *Nano Lett.* **11**, 2584-2589 (2011).
 11. Ueda, K., Tabata, H., & Kawai, T. Magnetic and electric properties of transition-metal-doped ZnO films. *Appl. Phys. Lett.* **79**, 987-990 (2001).
 12. Venkatesan, M., Fitzgerald, C. B., Lunney, J.G., & Coey, J. M. D. Anisotropic Ferromagnetism in Substituted Zinc Oxide. *Phys. Rev. Lett.* **93**, 177206 (2004).
 13. Takahashi, M. Magnetic and transport properties of degenerate ferromagnetic semiconductor EuO. *Phys. Rev. B* **93**, 235201 (2016).
 14. Sutarto, R., Altendorf, S. G., Coloru, B., Sala, M. M., Haupricht, T., Chang, C. F., Hu, Z., Schubler-Langeheine, C., Hollmann, N., Kierspel, H., Mydosh, J. A., Hsieh, H. H., Lin, H.-J., Chen, C. T., & Tjeng, L. H. Epitaxy, stoichiometry, and magnetic properties of Gd-doped EuO films on YSZ (001). *Phys. Rev. B* **80**, 085308 (2009).
 15. Maiorero, T., Schmehl, A., Melville, A., Heeg, T., Canella, L., Boni, P., Zander, W., Schubert, J., Shai, D. E., Monkman, E. J., Shen, K. M., Schlom, D. G., & Mannhart, J. Is There an Intrinsic Limit to the Charge-Carrier-Induced Increase of the Curie Temperature of EuO? *Phys. Rev. Lett.* **105**, 257206 (2010).
 16. Berger, C., Song, Z., Li, X., Wu, X., Brown, N., Naud, C., Mayou, D., Li, T., Hass, J., Marchenkov, A. N., Conrad, E. H., First, P. N., & de Heer, W. A. Electronic Confinement and Coherence in Patterned Epitaxial Graphene. *Science* **312**, 1191-1196 (2006).
 17. Tao, C., Jiao, L., Yazyev, O. V., Chen, Y.-C., Feng, J., Zhang, X., Capaz, R. B., Tour, J. M., Zettl, A., Louie, S. G., Dai, H., & Crommie, M. F. Spatially resolving edge states of chiral graphene nanoribbons. *Nat. Phys.* **7**, 616-620 (2011).
 18. Li, Y. Y., Chen, M. X., Weinert, M., & Li, L. Direct experimental determination of

- onset of electron-electron interactions in gap opening of zigzag graphene nanoribbons. *Nat. Commun.* **5**, 4311 (2014).
19. Magda, G. Z., Jin, X., Hagymasi, I., Vancso, P., Osvath, Z., Nemes-Incze, P., Hwang, C., Biro, L. P., & Tapasztó, L. Room temperature magnetic order on zigzag edges of narrow graphene nanoribbons. *Nature* **514**, 608-611 (2014).
 20. Zhang, Y., Li, S. Y., Huang, H. Q., Li, W. T., Qiao, J. B., Wang, W. X., Yin, L. J., Bai, K. K., Duan, W. H., & He, L. Scanning Tunneling Microscopy of the π Magnetism of a Single Carbon Vacancy in Graphene. *Phys. Rev. Lett.* **117**, 166801 (2016).
 21. Yazyev, O. V., & Helm, L. Defect-induced magnetism in graphene. *Phys. Rev. B* **75**, 125408 (2007).
 22. Ugeda, M. M., Brihuega, I., Guinea, F., & Gómez-Rodríguez, J. M. Missing Atom as a Source of Carbon Magnetism. *Phys. Rev. Lett.* **104**, 096804 (2010).
 23. Ugeda, M. M., Fernández-Torre, D., Brihuega, I., Pou, P., Martínez-Galera, A. J., Pérez, R., & Gómez-Rodríguez, J. M. Point Defects on Graphene on Metals. *Phys. Rev. Lett.* **107**, 116803 (2011).
 24. Gonzalez-Herrero, H., Gomez-Rodriguez, J. M., Mallet, P., Moaied, M., Palacios, J. J., Salgado, C., Ugeda, M. M., Veuillen, J.-Y., Yndurain, F., & Brihuega, I. Atomic-scale control of graphene magnetism by using hydrogen atoms. *Science* **352**, 437-441 (2016).
 25. Nair, R. R., Sepioni, M., Tsai, I., Lehtinen, O., Keinonen, J., Krasheninnikov, A. V., Thomson, T., Geim, A. K., & Grigorieva, I. V. Spin-half paramagnetism in graphene induced by point defects. *Nat. Phys.* **8**, 199-202 (2012).
 26. Wei, P., Lee, S., Lemaitre, F., Pinel, L., Cutaia, D., Cha, W., Katmis, F., Zhu, Y., Heiman, D., Hone, J., Moodera, J. S., & Chen, C.-T. Strong interfacial exchange field in graphene/EuS heterostructure. *Nat. Mater.* **15**, 711-716 (2016).
 27. Wang, Z., Tang, C., Sachs, R., Barlas, Y., & Shi, J. Proximity-induced ferromagnetism in graphene revealed by the anomalous Hall effect. *Phys. Rev. Lett.* **114**, 016603 (2015).
 28. Han, W., Kawakami, R. K., Gmitra, M., & Fabian, J. Graphene spintronics. *Nat.*

Nano. **9**, 794-807 (2014).

29. Khomyakov, P. A., Giovannetti, G., Rusu, P. C., Brocks, G., Van den Brink, J., & Kelly, P. J. First-principles study of the interaction and charge transfer between graphene and metals. *Phys. Rev. B* **79**, 195425 (2009).
30. Yu, Q., Lian, J., Siriponglert, S., Li, H., Chen, Y. P., & Pei, S. Graphene segregated on Ni surfaces and transferred to insulator. *Appl. Phys. Lett.* **93**, 113103 (2008).
31. Liu, N., Fu, L., Dai, B., Yan, K., Liu, X., Zhao, R. -Q, Zhang, Y. -F, & Liu, Z. -F. Universal Segregation Growth Approach to Wafer-Size Graphene from Non-Noble Metals. *Nano Lett.* **11**, 297-303 (2011).
32. Kim, K. S., Zhao, Y., Jang, H., Lee, S. Y., Kim, J. M., Kim, K. S., Ahn, J. H., Kim, P., Choi, J. Y., & Hong, B. H. Large-scale pattern growth of graphene films for stretchable transparent electrodes. *Nature* **457**, 706-710 (2009).
33. Ferrari, A. C., Meyer, J. C., Scardaci, V., Casiraghi, C., Lazzeri, M., Mauri, F., Piscanec, S., Jiang, D., Novoselov, K. S., Roth, S., & Geim, A. K. Raman Spectrum of Graphene and Graphene Layers. *Phys. Rev. Lett.* **97**, 187401 (2006).
34. Giovannetti, G., Khomyakov, P. A., Brocks, G., Karpan, V. M., Van den Brink, J., & Kelly, P. J. Doping Graphene with Metal Contacts. *Phys. Rev. Lett.* **101**, 026803 (2008).
35. Bai, K. K., Wei, Y. C., Qiao, J. B., Li, S. Y., Yin, L. J., Yan, W., Nie, J. C., & He, L. Detecting giant electron-hole asymmetry in a graphene monolayer generated by strain and charged-defect scattering via Landau level spectroscopy. *Phys. Rev. B* **92**, 121405(R) (2015).
36. Tian, J., Cao, H., Wu, W., Yu, Q., Guisinger, N. P., & Chen, Y. P. Graphene Induced Surface Reconstruction of Cu. *Nano Lett.* **12**, 3893-3899 (2012).
37. Kiraly, B., Iski, E. V., Mannix, A. J., Fisher, B. L., Hersam, M. C., & Guisinger, N. P. Solid-source growth and atomic-scale characterization of graphene on Ag(111). *Nat. Commun.* **4**, 1965 (2013).
38. Ugeda, M. M., Fernández-Torre, D., Brihuega, I., Pou, P., Martínez-Galera, A. J., Pérez, R., & Gómez-Rodríguez, J. M. Point Defects on Graphene on Metals. *Phys. Rev. Lett.* **107**, 116803 (2011).

39. Xiao, D., Yao, W., Niu, Q., Valley-contrasting physics in graphene: magnetic moment and topological transport. *Phys. Rev. Lett.* **99**, 236809 (2007).
40. Giovannetti, G., Khomyakov, P. A., Brocks, G., Kelley, P. J., van den Brink, J. Substrate-induced band gap in graphene on hexagonal boron nitride: Ab initio density functional calculations. *Phys. Rev. B* **76**, 073103 (2007).
41. Chen, Z.-G., Shi, Z., Yang, W., Lu, X., Lai, Y., Yan, H., Wang, F., Zhang, G., Li, Z. Observation of an intrinsic bandgap and Landau level renormalization in graphene/boron-nitride heterostructures. *Nat. Commun.*, **5**, 4461 (2014).
42. Andrei, E. Y., Li, G. H., Du, X. Electronic properties of graphene: a perspective from scanning tunneling microscopy and magnetotransport. *Rep. Prog. Phys.* **75**, 056501 (2012).
43. Wang, W. X., Yin, L. J., Qiao, J. B., Cai, T. C., Li, S. Y., Dou, R. F., Nie, J. C., Wu, X. S., He, L. Atomic resolution imaging of the two-component Dirac-Landau levels in a gapped graphene monolayer. *Phys. Rev. B* **92**, 165420 (2015).
44. Bode, M. Spin-polarized scanning tunnelling microscopy. *Rep. Prog. Phys.* **66**, 523–582 (2003).
45. Wiesendanger, R. Spin mapping at the nanoscale and atomic scale. *Rev. Mod. Phys.* **81**, 1495-1550 (2009).
46. Chen, H., Xiao, W., Wu, X., Yang, K., Gao, H. *J. Vac. Sci. Technol. B* **32**, 061801 (2014).
47. Rastei, M. V., Bucher, J. P. Spin polarized tunnelling investigation of nanometer Co clusters by means of a Ni bulk tip. *J. Phys.: Condens. Matter* **18**, L619-L624 (2006).
48. Yang, L., Park, C.-H., Son, Y.-W., Cohen, M. L., Louie, S. G. Quasiparticle energies and band gaps in graphene nanoribbons. *Phys. Rev. Lett.* **99**, 186801 (2007).
49. Si, C., Duan, W., Liu, Z., & Liu, F. Electronic Strengthening of Graphene by Charge Doping. *Phys. Rev. Lett.* **109**, 226802 (2012).

Acknowledgments

This work was supported by the National Natural Science Foundation of China (Grant Nos. 11674029, 11422430, 11374035, 11334006), the National Basic Research

Program of China (Grants Nos. 2014CB920903, 2013CBA01603), the program for New Century Excellent Talents in University of the Ministry of Education of China (Grant No. NCET-13-0054). L.H. also acknowledges support from the National Program for Support of Top-notch Young Professionals and support from “the Fundamental Research Funds for the Central Universities”.

Author contributions

Y.Z. synthesized the samples and performed the experiments. L.H. and Y.Z. analyzed the data. X.L.S. and W.H.D. performed the theoretical calculations. L.H. conceived and provided advice on the experiment, analysis, and theoretical calculation. L.H. and Y.Z. wrote the paper. All authors participated in the data discussion.

Figures

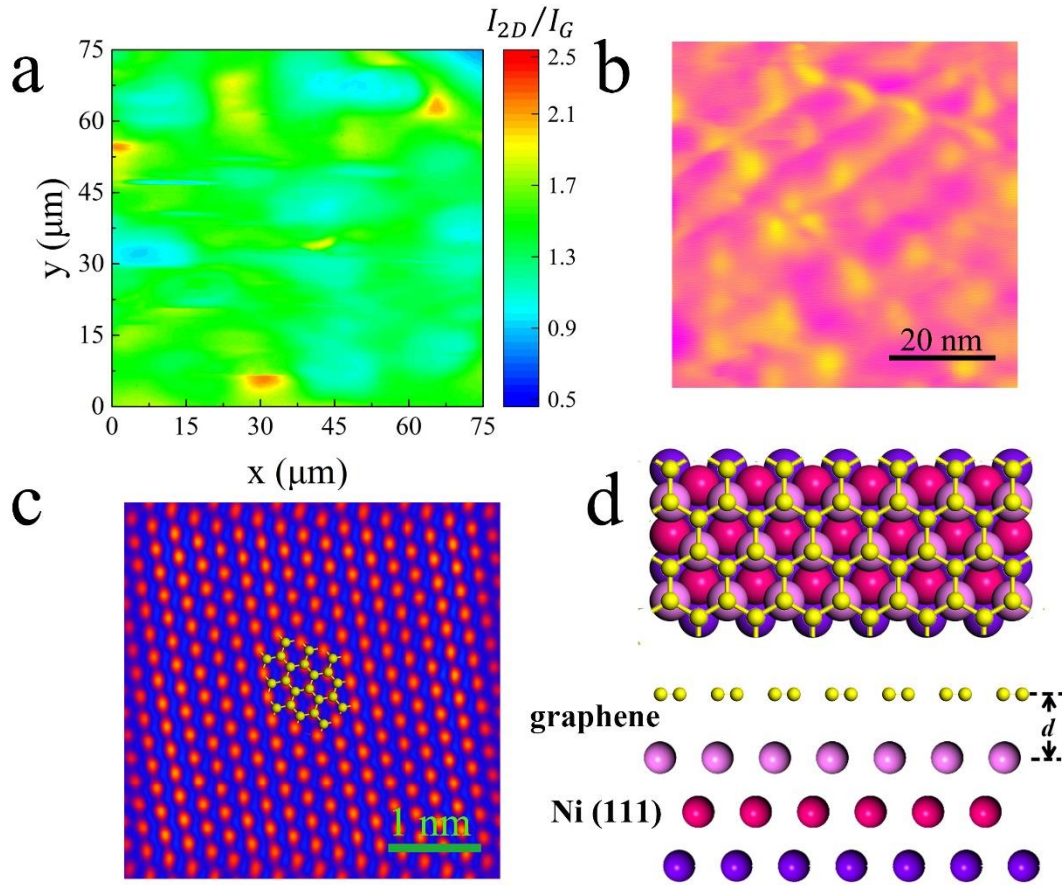


Figure 1. Graphene monolayer on Ni (111) surface. **a.** $75\ \mu\text{m} \times 75\ \mu\text{m}$ Raman mapping of the intensity ratio I_{2D}/I_G of the graphene transferred on a SiO_2/Si substrate. In graphene, the peak of the 2D band and G band are at $\sim 2700\ \text{cm}^{-1}$ and $\sim 1580\ \text{cm}^{-1}$ of the Raman spectrum respectively. The intensity ratio of them can reflect the layer numbers of graphene, and usually $I_{2D}/I_G > 1$ can be regarded as the graphene monolayer. **b.** $60\ \text{nm} \times 60\ \text{nm}$ STM topographic images of graphene monolayer on a Ni foil ($V_b = 0.3\ \text{V}$, $I = 0.2\ \text{nA}$). **c.** Zoom-in $4\ \text{nm} \times 4\ \text{nm}$ atomic resolution STM image of graphene, showing the triangular lattice of the monolayer graphene on Ni (111) surface ($V_b = 0.3\ \text{V}$, $I = 0.2\ \text{nA}$). **d.** Schematic representation of graphene monolayer on Ni (111) surface. The carbon atoms of the A sublattice are on top of the Ni atoms of the topmost atomic layer, while atoms of the B sublattice are located above the hollow sites of the topmost atomic layer of Ni.

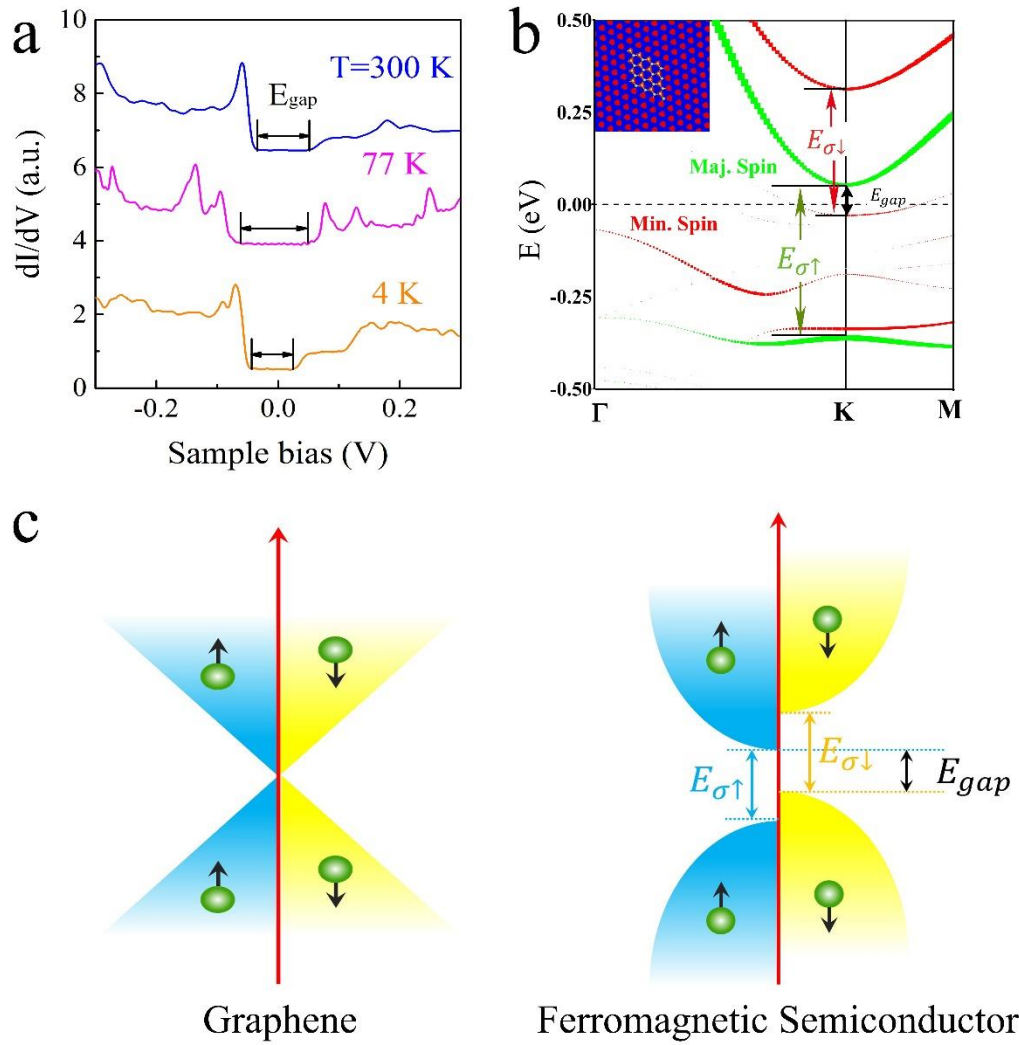


Figure 2. Microscopic properties of the graphene monolayer on Ni (111) surface. a. Representative STS spectra of the graphene on Ni (111) surface recorded at 4 K and, 77 K, and 300 K, respectively. **b.** Band structures of graphene monolayer adsorbed upon Ni (111) surface. The Fermi level is at zero energy. The labels Maj. Spin and Min. Spin indicate the majority-spin bands (green lines) and minority-spin bands (red lines) of the graphene monolayer on Ni, respectively. Inset: DFT-simulated STM image of the graphene monolayer on Ni (111) surface. **c.** (Left) Low-energy electronic band structure of graphene monolayer. The electronic structures for the spin-up and spin-down states are degenerate. (Right) Schematic band structure of the ferromagnetic semiconductor. In this work, strong interaction between graphene and a magnetic metal (Ni) leads to a band gap and spin splitting simultaneously in graphene, which makes the graphene monolayer a ferromagnetic semiconductor.

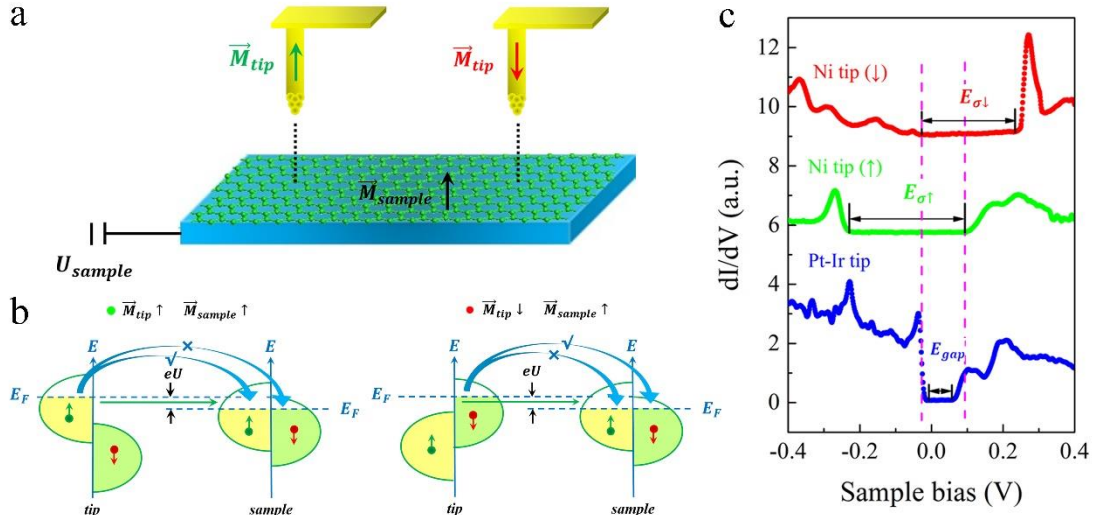


Figure 3. Spin-polarized dI/dV spectra of the graphene monolayer on Ni (111) surface. **a.** Schematic experimental set-up of spin-polarized STM. Spins of the sample aligned perpendicular to the sample surface can be detected by the Ni tip along the tip axis. **b.** Principle of spin-polarized tunnelling between magnetic electrodes that exhibit a parallel ($\vec{M}_{tip} \uparrow, \vec{M}_{sample} \uparrow$ green dot) and an antiparallel ($\vec{M}_{tip} \downarrow, \vec{M}_{sample} \uparrow$ red dot) magnetization. The spin is conserved during the elastic electron tunnelling. **c.** Spin-polarized dI/dV spectra of the graphene monolayer on Ni surface. The red curve is measured when the tip polarization \vec{M}_{tip} and the magnetization of the sample \vec{M}_{sample} are antiparallel, which reflects the LDOS of the spin-down electrons. The green curve is measured when the \vec{M}_{tip} and \vec{M}_{sample} are parallel, which reflects the LDOS of the spin-up electrons. The blue dots are the dI/dV spectrum of graphene on Ni surface measured via a Pt/Ir tip.

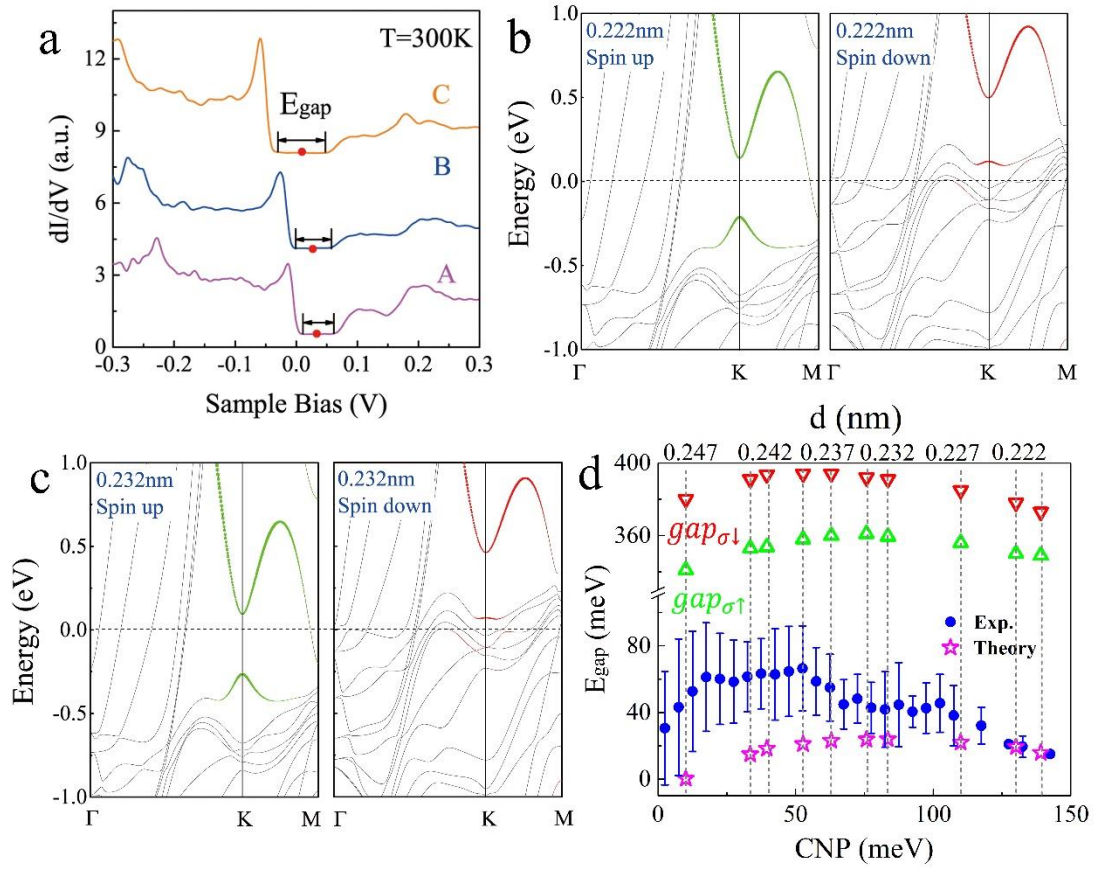


Figure 4. Electronic properties of the graphene monolayer on Ni (111) surface at 300 K. **a.** Representative STS spectra recorded at different positions of the graphene monolayer on Ni (111) surface at 300 K. The CNPs at different positions of the graphene are given by red dots in the spectra. **b-c.** Calculated band structures of the graphene monolayer on Ni (111) surface. The Fermi level is set at zero, and the green and red lines are the majority- and minority-spin bands of the graphene monolayer, respectively. The labels σ_{\uparrow} and σ_{\downarrow} indicate the majority- and minority-spin bands of the graphene monolayer on Ni (111) surface. **d.** Solid blue dots show the measured gap as a function of the CNP deduced from thousands of the STS data recorded at different positions in our experiment. The simulated relationships among the band gap, the CNP, and the distance between the graphene monolayer and Ni (111) surface are also summarized in this figure for comparison.